


Low-field vortex melting in a single crystal of $\text{Ba}_{0.6}\text{K}_{0.4}\text{Fe}_2\text{As}_2$

Ankit Kumar¹,¹ Sayantan Ghosh,¹ Tsuyoshi Tamegai,² and S. S. Banerjee^{1,*}

¹*Department of Physics, Indian Institute of Technology, Kanpur 208016, India*

²*Department of Applied Physics, The University of Tokyo, Hongo, Bunkyo-ku, Tokyo 113-8656, Japan*

 (Received 12 October 2018; revised manuscript received 2 December 2019; published 7 January 2020)

Theoretically, the vortex melting phenomenon occurs at both low and high magnetic fields at a fixed temperature. While the high-field melting has been extensively investigated in high- T_c cuprates, the low-field melting phenomena in the presence of disorder has not been well explored. Using bulk magnetization measurements and a high-sensitivity differential magneto-optical imaging technique, we detect a low-field vortex melting phenomenon in a single crystal of $\text{Ba}_{0.6}\text{K}_{0.4}\text{Fe}_2\text{As}_2$. The low-field melting is accompanied with a significant change in local magnetization, ~ 3 G, which decreases with increasing applied field. The observed vortex melting phenomenon is traced on a field-temperature phase diagram, which lies very close to theoretically predicted Lindemann criteria based low-field melting line. Our analysis shows a Lindemann number $c_L = 0.14$ associated with the low-field melting. Imaging of low-field vortex melting features shows that the process nucleates via formation of extended fingerlike projections which spreads across the sample with increasing field or temperature, before entering into an interaction-dominated vortex solid phase regime. Magnetization scaling analysis and angular dependence of bulk magnetization hysteresis loop shows extended pins naturally present in the sample. These defects create a low-field glassy vortex phase sustaining a finite critical current present in the phase diagram below the low-field liquid phase. We construct a vortex matter phase diagram, which identifies boundaries demarcating a low-field glassy vortex state from a dilute vortex liquid phase and a weakly interacting solid phase above it. All these phases are shown to be present well below the interaction dominated vortex state shown in the phase diagram.

DOI: [10.1103/PhysRevB.101.014502](https://doi.org/10.1103/PhysRevB.101.014502)

I. INTRODUCTION

A conventional, ordered atomic lattice with long-range positional order exhibits a first-order thermal melting into a liquid phase. The presence of quenched random disorder in the lattice leads to loss of positional order thereby suppressing the first-order nature of this melting transition. The vortex state in type-II superconductors is a convenient prototype for studying the behavior of phase transitions in a soft condensed-matter system in the presence of thermal fluctuations and pinning effects. In the context of vortices, their pinning by defects and impurity sites in a superconductor is technologically important as the pins immobilize vortices driven by electric currents, thereby reducing the vortex flow induced dissipation. Pinning leads to loss of long-range order in a vortex solid [1]. Thermal fluctuations often counter pinning effects by thermally activating vortices out of the pinning centers thereby effectively weakening the pinning potential. In the soft vortex state, the competition between intervortex interactions trying to generate an ordered vortex configuration and pinning and thermal fluctuations trying to destroy long-range order in the vortex state leads to a variety of different static vortex matter phase [1–14]. In pinned vortex solids the positional correlations between vortices decay either algebraically or exponentially [1,11,13,14], and they are called Bragg or vortex glass phases respectively. The elastic moduli

of the vortex solid are magnetic field (B) dependent [1]. At low B when the intervortex spacing $a_0(\propto\sqrt{\phi_0/B}) > \lambda$ (where λ is the superconducting penetration depth and ϕ_0 is the magnetic flux quantum), the elastic moduli of the lattice are small due to weak intervortex interactions. Due to nonlocal effects, the elastic moduli also decreases at high B where $a_0 \ll \lambda$. At intermediate magnetic field strengths where the elastic moduli take maxima, the vortex solid phase is stabilized. The softening of elastic moduli triggers a thermally induced melting phenomenon in the vortex solid. Thermal fluctuations acting on a soft vortex solid melt it into a vortex liquid phase, wherein the positional correlations exist only between nearest-neighbor vortices. Conventionally, a popular criterion to describe melting is the Lindemann criterion [1], $\sqrt{\langle u^2 \rangle} \sim c_L a_0$, where $\sqrt{\langle u^2 \rangle}$ is the rms deviation of the vortex line from its equilibrium position due to thermal fluctuations, and $c_L \sim 0.1-0.2$ is the empirical choice of the Lindemann number. Using such a Lindemann criterion and softening of the elastic moduli of the vortex solid, the boundary of stability of the vortex solid phase in a field (B)–temperature (T) phase diagram is derived. It was shown that in a pinning-free system, the vortex solid melts into a vortex liquid phase at both high and low B [1,3,15]. Thus, a unique characteristic of the B - T vortex matter phase diagram is that the phase boundary, across which the continuous symmetry of the vortex liquid phase is broken as it forms a vortex lattice, is encountered not only at high but also at low B . High- T_c superconductors (HTSCs) with their enhanced T_c , large anisotropy, and their complex vortex structure, comprised of a string of interacting

*satyajit@iitk.ac.in

two-dimensional vortices [1,14], became popular systems for studying the vortex solid to liquid melting phenomena [6–9,11,16,17] at high B . At high B , the vortex solid to liquid transformation was shown to be like an ice-to-water-like transformation wherein the vortex liquid is relatively denser compared to the solid phase (vortex density, $\rho = B/\phi_0$) [18,19]. Conventionally it is believed that the presence of quenched random disorder leads to loss of positional correlations in the vortex lattice thereby obliterating all evidence of a melting phenomenon [20–22]. While overall melting features can be understood via the Lindemann criterion, the vortex dimensionality also plays an important role in governing this phenomenon. It has been proposed that melting from a one-dimensional (1D) stack of two-dimensional (2D) vortices into a 2D vortex liquid phase occurs as enhanced thermal fluctuations either overcomes the coupling between the 2D vortices in the stack [20] or by disrupting the net intervortex interactions within a stack [22]. While numerous studies exist on investigating the vortex solid melting phenomenon at high vortex densities (high B), comparatively fewer studies exist on dilute vortex melting. As per conventional understanding, pinning effects should dominate at low fields; hence, the dilute vortex solid at low fields is likely to be strongly pinned and configurationally disordered. Hence, one may ask, in such disordered vortex solids, is there a chance of vortex melting at low fields? Experimentally it is not quite well established if a pinned vortex solid melts at low B in realistic samples with pinning. Some recent studies in clean HTSCs at low fields have suggested the presence of high vortex mobility regions and changes in local vortex density at low B [23,24]. However, apart from HTSCs which have a complex vortex structure, there exists no evidence of melting at low B in any other materials. It may be mentioned that in the dilute regime melting signatures are masked by the presence of strong magnetization irreversibility induced by strong pinning effects. In fact, at low fields, theoretically, the presence of a pinned glassy vortex phase has been proposed in the past, viz., “the reentrant glass” [12].

In recent times, the pnictides class of superconductors has been extensively investigated. These materials possess moderately high T_c 's, small superconducting coherence length (ξ), and moderate anisotropy, which makes the vortex state in these materials potentially susceptible to thermal fluctuations. Theories have predicted the vortex solid melting phenomenon in different pnictide materials, like, $\text{LaFeAsO}_{1-x}\text{F}_x$, $\text{Ba}(\text{Fe}_{1-x}\text{Co}_x)_2\text{As}_2$, and $\text{Nd}(\text{O}_{1-x}\text{F}_x)\text{FeAs}$ [25,26]. A source of complication in pnictide materials towards experimentally observing signatures of thermal melting of the vortex solid is that they usually possess very strong pinning. It is known that pinning induced irreversibility masks signatures related to the vortex melting phenomenon, such as changes in equilibrium magnetization associated with a change in vortex density as the vortex solid transforms into a liquid [27]. Most imaging studies on the vortex state in pnictide superconductors report a disordered vortex solid which persists up to high B [28,29], confirming the presence of strong pinning in this class of superconductors. Studies suggest the presence of microscopic chemical inhomogeneities in the system to act as point pinning centers in the material [30]. However, a recent study in K-doped 122 systems, viz., $\text{Ba}_{0.6}\text{K}_{0.4}\text{Fe}_2\text{As}_2$

has shown the presence of an ordered vortex solid present at high field [31], where presumably the intervortex interactions have managed to overcome the vortex pinning strength in this material. It has also been reported that $\text{Ba}_{0.5}\text{K}_{0.5}\text{Fe}_2\text{As}_2$ shows thermodynamic signatures of vortex melting at high fields [32]. In this paper, we explore signatures of a vortex liquid phase at low B in a single crystal of $\text{Ba}_{0.6}\text{K}_{0.4}\text{Fe}_2\text{As}_2$. We find that at low fields, while effective pinning is large, the pinning strength is distributed between weak and strong pins. At low B , we observe a change in equilibrium local magnetization ~ 3 G, which is associated with a melting transition. Using the high sensitivity differential magneto-optical imaging technique to spatially map the location of changes in local B , we show that low-field melting begins as linear fingerlike fronts projecting into the sample from different locations on the sample edge. Eventually, they spread all across the sample before merging into each other as B or T is increased. We show that due to nucleation of vortex liquid at the sample edges, the edge screening currents redistribute in a way that it partially flows along the sample edge and part along the interface between vortex solid and liquid phases creating regions with suppressed vortex density inside the sample. The vortex melting transition is located in a B - T phase diagram which lies in close proximity to the theoretically proposed low-field melting line based on a Lindemann melting criterion also plotted in the phase diagram. Using magnetization scaling analysis and angular dependent magnetization, we show the presence of elongated defects extending along the sample thickness naturally present in the sample. These extended defects produce a low-field glassy vortex state below the low-field vortex liquid phase in the phase diagram. In a field and temperature vortex matter phase diagram, we identify the low-field dilute vortex liquid phase and demarcate it from the low-field glassy vortex phase. At higher fields, the vortex liquid phase transforms into a weakly interacting vortex solid. We show that all these different phases are present below the intervortex interaction dominated boundary.

II. EXPERIMENT

We report results on a single crystal of $\text{Ba}_{0.6}\text{K}_{0.4}\text{Fe}_2\text{As}_2$ with dimensions $1.7 \times 1.2 \times 0.025$ mm³ and $T_c = 38$ K chosen from a batch grown using a self-flux method in Al_2O_3 crucibles [33]. In our experiments, the applied magnetic field (B_a) was maintained parallel to the crystallographic c axis. Bulk magnetization measurements were performed in a commercial Cryogenic superconducting quantum interference device magnetometer. For imaging the distribution of the local magnetic field component (which is proportional to the local vortex density) parallel to the crystallographic c axis (B_z) across the sample, we use conventional magneto-optical imaging (MOI). We also use high sensitivity differential magneto-optical (DMO) imaging technique to measure changes in local vortex density (δB_z). Details of both MOI and DMO techniques are discussed elsewhere [21,34–36]. Briefly, in MOI we image the Faraday rotated light intensity distribution [$I(x, y)$] of linearly polarized light reflected from the sample, where $I(x, y) \propto B_z^2(x, y)$; note that the B_z direction is parallel to B_a and the coordinates (x, y) are along the sample surface.

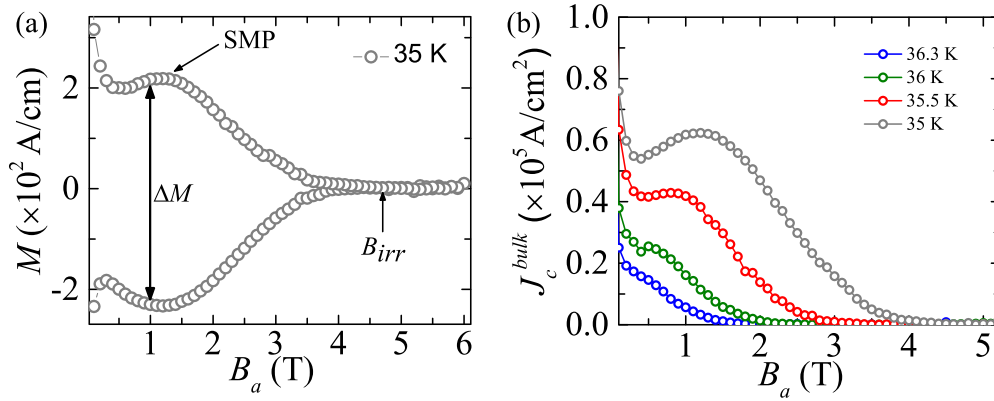


FIG. 1. (a) DC magnetization (M - B_a curve) loop measured in a single crystal of $\text{Ba}_{0.6}\text{K}_{0.4}\text{Fe}_2\text{As}_2$ with $T_c = 38$ K for applied magnetic field $B_a \parallel$ crystallographic c axis at 35 K. The second magnetization peak anomaly (SMP) is seen to develop at $B_a \sim 0.4$ T and extends up to 1.2 T. Here we have chosen the symbol size comparable to the size of the error bars. (b) Critical current density J_c^{bulk} vs applied field measured at different temperatures are plotted.

In a DMO technique for the same B_a , we obtain an image which is the average of repeated differential image captured at $B_a = (\text{MO images captured at } B_a + \delta B_a) - (\text{MO image at } B_a)$ with $\delta B_a = 1$ G. The intensity distribution in the differential image $\delta(x, y)$ in the DMO images was calibrated to map the changes in the local magnetic field $\delta B_z(x, y)$ produced at different locations inside the sample in response to the external field modulation of $\delta B_a = 1$ G.

III. RESULTS AND DISCUSSION

Figure 1(a) shows the bulk magnetization hysteresis loop measurement at 35 K. The hysteresis loop width ΔM is related to the pinning strength experienced by the vortices inside the superconductor. Figure 1(a) shows that ΔM undergoes a modulation due to the presence of a second magnetization peak (SMP) anomaly in this sample. The SMP anomaly in magnetization has been seen in HTSCs [37–45] as well as in different low- T_c superconductors, for example in $2H\text{-NbSe}_2$ [46,47] and also in $\text{Ba}_{0.6}\text{K}_{0.4}\text{Fe}_2\text{As}_2$ [48,49], apart from other iron-based superconductors [50–53]. Small-angle neutron-scattering investigations of the SMP anomaly in $\text{Ba}_{0.64}\text{K}_{0.36}\text{Fe}_2\text{As}_2$ show that this anomaly is associated with an order to disorder transition in the vortex state precipitated by proliferation of topological defects in the vortex state at high B_a [49]. We would like to mention that all our investigations are performed in a B_a regime which is far below the SMP regime which typically begins from 0.4 T (where there is a minima in J_c^{bulk}) and extends up to 1.2 T (where the J_c^{bulk} peaks).

We estimate J_c^{bulk} from ΔM [see Fig. 1(a)] using [54,55] $J_c^{\text{bulk}} = 20\Delta M/[a(1 - a/3b)]$, and a and b ($b > a$) are the crystal dimensions perpendicular to B_a . The $J_c^{\text{bulk}}(B_a)$ behavior overall has a monotonically decreasing trend with increasing B_a as shown in Fig. 1(b) and also shows a broad bump associated with SMP. Note that the J_c^{bulk} 's value at low B_a is high in the range of $\sim 10^4$ A/cm² even at $T_s > 0.9T_c$, where one expects large thermal fluctuations to suppress pinning effects significantly. This suggests the presence of strong pinning in the sample.

Figure 2(a) shows $B_z(x)$ measured across the line drawn in Fig. 2(b) (black line in 30 G image) at different B_a . The B_z near the sample edges is seen to be enhanced due to strong shielding currents circulating on the sample edges and the $B_z(x)$ near the sample center exhibits a non-Bean-like, dome-shaped profile. At high B_a [see $B_z(x)$ for $B_a = 200$ G in Fig. 2(a)], the uniform B_z distribution across the sample is associated with the uniform vortex density in a vortex solid phase. Two conventional MO images of the sample at 33.5 K and 11 and 30 G in the field-cooled (FC) state are shown in Fig. 2(b). Note that all measurements reported here are for the sample in a field-cooled state. Returning to the dome shape of the B_z profile at lower fields, it is known that geometrical barriers induced presence of strong shielding currents near the sample edges [56] drive vortices away from the edges (where local B_z is low) and they collect near the sample center. Consequently, the B_z and hence the vortex density near the edges gets suppressed while the B_z in the sample interior develops a domelike feature [56–58] [see Fig. 2(a)]. In the $B_z(x)$ profile in Fig. 2(a), we see that between the sample center and near the left sample edge the $B_z(x)$ exhibits a significant dip. In fact, the region with suppressed B_z expands in the direction of sample center with increasing B_a [see within the black dashed circle in Fig. 2(a)]. Note also that there is an asymmetry of this dip feature between the left and right sample edges. This dip feature shows the shielding currents getting stronger with increasing B_a , resulting in a significant number of vortices being pushed away from the sample edges. In Fig. 2(b) the MO image at 33.5 K and at an applied field of 30 G shows that the regions with suppressed $B_z(x)$ have a darker MO contrast compared to the surroundings. By numerically inverting [59] the measured $B_z(x, y)$ distribution at $B_a = 11$ G and at $T = 33.5$ K [Fig. 2(c)], we estimate the shielding current distribution $|J_s(x)|$ near the left edge of the sample [along the red line shown in Fig. 2(b) in the 11 G image]. For clarity, the current distribution only near one edge of the sample is shown in Fig. 2(c). The $|J_s(x)|$ in Fig. 2(c) fits the expression [56,60] for shielding currents, $J_s(x) = B_a(w - 2x)/(d\sqrt{x(w - x)})$, where w is the sample width, d is the sample thickness, and B_a is the applied magnetic field. Using the fit, the shielding currents in the sample

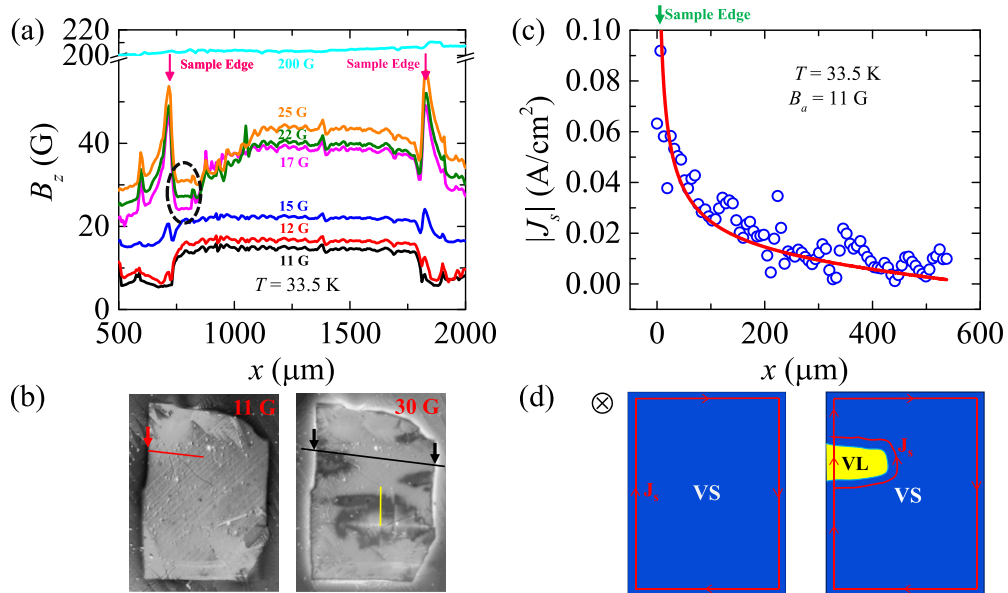


FIG. 2. Panel (a) shows the B_z profile along the black line drawn in (b) (conventional MO image at 30 G) at 33.5 K and at different applied magnetic field from 11 to 200 G. Note that far away from the sample edges (beyond the scale shown in the figure) local field B_z reduces to applied field B_a . Positions of the sample edges are indicated in the plot. Dashed black circular region in the plot shows the depletion of vortex density (or lowering of B_z). Panel (b) shows the MO images taken at 33.5 K and at applied field of 11 and 30 G respectively. (c) Screening current inside the sample obtained by inverting the conventional MO image acquired at an applied field of 11 G and temperature 33.5 K is plotted. Red curve shows the fitting through the data using the equation $J_s(x) = B_a (w - 2x)/(d\sqrt{x(w-x)})$ (where J_s is the shielding current, w is the sample width, d is the sample thickness, and B_a is the applied magnetic field). Current distribution only in the half sample [see red line drawn in Fig. 2(b) in 11 G image] has been shown here with maximum current at the edge as shown in the figure. Here we have chosen the symbol size comparable to the size of the error bars. (d) The left schematic shows the screening current J_s (red line) flowing at the edges of the sample in the presence of an applied magnetic field (\otimes mentions the direction of the magnetic field is going into the plane for both schematics). Right side schematic shows the formation of a vortex liquid puddle nucleated at the sample edge. The schematic on the right shows the shielding current redistributes by partially flowing along the sample edge and partially circulating along the boundary between the VL puddle and the VS phase. Note that the schematic is only a representation relating to the formation of solid-liquid interface and the distribution of currents in this region (the schematic is not to scale). All the measurements have been done in the field-cooled state with the magnetic field applied parallel to the crystal c axis.

near the edges are $J_s \sim 10^{-1} \text{ A/cm}^2 \ll J_c^{\text{bulk}} \sim 10^4 \text{ A/cm}^2$ [determined from bulk $M(B_a)$ measurements in Figs. 1(a) and 1(b)]. This apparent inconsistency is reconciled by considering that the distribution of pinning strength in the sample is not uniform, and the sample has strong and weak pinning centers with the strong pinning centers dominating the bulk magnetization hysteretic response measurement. We believe that these strong pinning centers which dominate the bulk $M(B_a)$ response are strong enough to survive up to high T near T_c . On the other hand, the weak pinning centers have a low J_c such that $J_s \sim 10^{-1} \text{ A/cm}^2$ is enough to depin vortices and push them away from these regions in the sample. The asymmetry in the suppressed B_z feature between the left and right sample edges is related to nonuniformity of the pinning distribution across the sample. One possible cause for the observation of bright magneto-optical contrast over the fingerlike projections at 30 G ($T = 33.5 \text{ K}$) in the MO image of Fig. 2(b) is related to enhanced density of trapped vortices pinned in strongly pinned regions of the sample. If this was a valid possibility then, we should have observed this brightening feature down to low fields like 11 G at 33.5 K for the FC state. However, in Fig. 2(b) we do not see the brightening features down to 11 G. Furthermore, if the brightening appearing in the MO image at

30 G in Fig. 2(b) was related to a strong pinning region, then such strong pinning regions should shield out modulations of external magnetic field. Hence, the bright regions in Fig. 2(b) at 30 G should exhibit negligible changes in local field (δB_z) in response to a modulation of the external field (for example see Fig. 3 of Ref. [21]). To explore this feature, we perform the differential magneto-optical imaging technique discussed below.

Figures 3(a) and 3(b) show DMO images obtained as a function of varying B_a at fixed $T = 33.5$ and 30.2 K, respectively, while Fig. 3(c) shows DMO images at fixed $B_a = 15 \text{ G}$ captured at different T . The gray shade in the images [Fig. 3(a)], changing from a whitish to blackish shade, represents variations in δB_z . Initially, for low fields at 10 G [not shown in Fig. 3(a) panel, but this feature is seen in Fig. 3(b) at 12 G], the whole sample has an almost uniform gray [blue in Fig. 3(b)] intensity. The gray regions [blue in Fig. 3(b)] have $\delta B_z = \delta B_a = 1 \text{ G}$, wherein the density of vortices follows the changes in the external magnetic field. As B_a is increased, bright [yellow in Fig. 3(b)] fingerlike regions begin invading the gray [blue in Fig. 3(b)] regions of the sample from different locations on the sample edges [e.g., see 25 and 36 G images in Figs. 3(a) and 3(b), respectively].

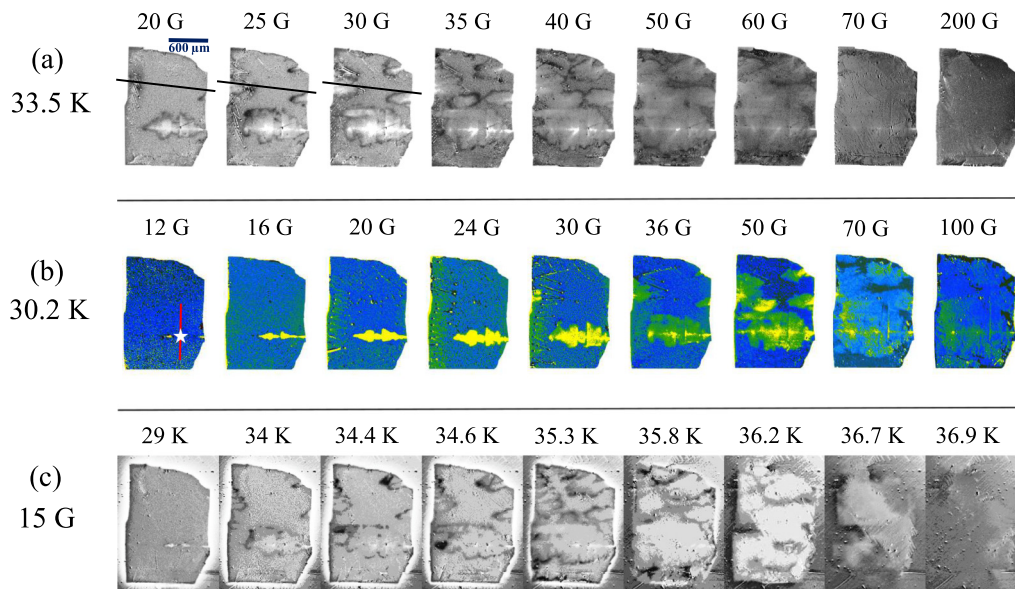


FIG. 3. (a),(b) Differential MO (DMO) images taken at 33.5 and 30.2 K respectively at different B_a . Panel (b) has been colored for better representation of the propagation of vortex melting across the sample. Some of the images in (b), e.g., 20, 24, and 30 G images, show a zigzag pattern at the left edge of the sample. This zigzag pattern is due to well-known Bloch walls seen on the magneto-optical film [61] which is placed on top of the sample for magneto-optical imaging. (c) Isofield differential MO images taken at a constant applied field of 15 G at varying temperature. In (a)–(c) gray [blue in (b)] region represents vortex density region $\delta B_z = \delta B_a = 1$ G and bright [yellow in (b)] region represents enhanced vortex density region with $\delta B_z > 1$ G (vortex liquid; VL). Note that contrast in all images has been enhanced compared to the raw images for better visibility of the features. However, all quantitative analyses involving B_z have been done using raw images. All the measurements have been done in the field-cooled state.

Notice that the bright regions in the DMO images occur in the same sample location where the brightening was seen in the 30 G conventional MO image in Fig. 2(b). These bright regions [yellow in Fig. 3(b)] are not symmetric patches but possess a directionality in their shape. Over the bright regions [yellow in Fig. 3(b)] in DMO images, the δB_z is larger than 1 G, and hence in these regions the local vortex density has changed more in comparison to other neighboring gray regions. In the vicinity of the enhanced local field, i.e., δB_z it may be noted that the $B_z(x)$ is non-Bean-like with a dome-shaped profile [see Fig. 2(a)]. Prior to the brightening observed over regions of the sample in the differential images, the $B_z(x)$ profile shows an almost uniform field distribution over these regions, suggesting that the feature is not associated with flux penetration. With increasing B_a , we see more such bright [yellow in Fig. 3(b)] linear fronts invading from the sample edges and expand after which they begin merging into each other at higher B_a [e.g., see 40 and 50 G images in Figs. 3(a) and 3(b), respectively]. As B_a increases and the bright fronts spread across the sample, they also become less bright. Note that at high B_a of 200 G [Fig. 3(a)] the δB_z over the sample again becomes uniform, namely $\delta B_z \sim 1$ G = δB_a . At these relatively high fields recall that Fig. 2(a) shows that the B_z distribution across the sample is uniform, viz., the vortex state has a uniform vortex density. The absence of any significant gradients in $B_z(x)$ at 200 G suggests this state is an ordered vortex solid phase (see video 1 in the Supplemental Material [62]). In the isofield DMO images in Fig. 3(c) we observe similar features of bright regions with enhanced δB_z developing and propagating across the sample with increasing T at constant B_a . Note from Fig. 3(c) that

the sample disappears uniformly at 36.9 K, suggesting the T_c is uniform across the sample and which in turn indicates the homogenous quality of the sample. We would like to mention that the bright regions appear at the same location in the sample at unique field and temperature values, which are independent of whether the measurement performed is an isothermal or isofield run. This suggests the thermodynamic nature of the change seen in these FC state measurements. We would like to mention that we are able to observe these features in the DMO measurements only up to $0.4T_c$. For $T < 0.4T_c$, the signature for the above transformation in the vortex state is masked by the irreversibility in the sample (as pinning strength enhances with decreasing T). Also note that at any high T and B_a above 200 G, we do not observe any change in local B_z appearing (we have measured up to 600 G). As mentioned earlier, strong pinning regions should exhibit dark contrast in DMO images due to their ability to screen external field modulation. Note that the regions where bright fingerlike projections appeared in the sample at 30 G in the conventional MO image in Fig. 2(b) is also the location where the DMO contrast becomes bright (see Fig. 3). The brightening of magneto-optical contrast in the DMO image of Fig. 3 relates to enhanced δB_z in response to the external field modulation of 1 G. Thus, the observed brightening in DMO signal is not correlated with enhanced shielding response. We conclude that the brightening in Fig. 2(b) at 30 G at the elevated temperature of 33.5 K is not related to strong pinning in those regions.

Figure 4(a) shows $\delta B_z(x)$ measured along the line drawn in Fig. 3(b) at different B_a for the 30.2 K data, with the plots artificially offset for the sake of clarity. The appearance of

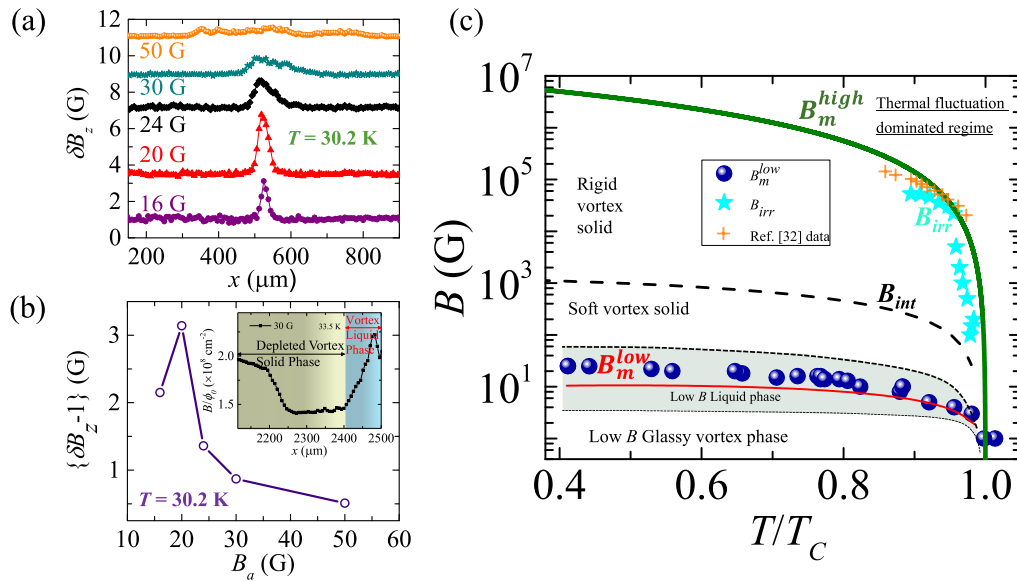


FIG. 4. (a) Local-field variation (δB_z) across the red line drawn in Fig. 3(b) is plotted (for 30.2 K). The $\delta B_z(x)$ plots are vertically shifted for the sake of clarity. Figure clearly shows with the increase in B_a there is an enhancement in the local field present on the sample at a position marked as * as shown in the first figure of Fig. 3(b). (b) Shows the field dependence of the peak value of δB_z above 1 G, viz., the $\{\delta B_z - 1\}$ at the location marked with * on the sample in the first figure of Fig. 3(b). Inset shows the variation in the number of vortices/cm² [across yellow line in Fig. 2(b)] in the conventional MO image taken at 33.5 K and at applied field of 30 G. (c) $B(T)$ phase diagram (blue color data) is plotted for the sample region marked as * in the first figure of Fig. 3(b). The red color solid line is a fit to the low-field melting line (B_m), Eq. (1) (see text below). A shaded region has been shown between two dashed lines to distinguish between a liquidlike phase from a low-field vortex glass and soft vortex solid phase at higher fields. Black dashed color line is the boundary of intervortex interaction $B_{int}(T)$ of the vortex matter. The olive color line is high-field melting line. Cyan color data is the irreversibility data $B_{irr}(T)$ obtained from M - B curve. + symbol represents the high-field melting data of $\text{Ba}_{0.5}\text{K}_{0.5}\text{Fe}_2\text{As}_2$ sample, from Ref. [32]. Different phases have been identified in the different field regime of the phase diagram. In all the plots, we have chosen the symbol size comparable to the size of the error bars.

the yellow regions at 16 G [see Fig. 3(b)] coincides with a change in δB_z of 2 G, while δB_z value is ~ 1 G ($=\delta B_a$) away from the yellow locations as discussed earlier in the context of Fig. 3. In Fig. 4(b), we plot the maximum value of $(\delta B_z - 1)$ G versus B_a at 30.2 K. Both Figs. 4(a) and 4(b) show that with increasing B_a , the magnitude of δB_z over the yellow region changes by about 3 G at $B_a = 20$ G before decreasing at higher B_a . Figure 4(a) shows that the width of these regions also gets broader with increasing B_a , which corresponds to the yellow regions spreading [see Fig. 3(b)]. Above $B_a = 50$ G the increase in δB_z above 1 G reduces to 0.5 G and weakens further, which corresponds to a gradual weakening of expanding yellow regions as the vortex matter becomes denser at larger B_a . It appears that over the yellow regions, the dilute vortex state exhibits a larger change in local vortex density corresponding to a phase change in the vortex matter. At 30 G, we determine the behavior of $B_z(x)$ at 33.5 K in Fig. 2(b) over the vertical yellow line. The vertical yellow line in Fig. 2(b) extends from the uniform gray regions in the sample up to the bright regions where this same bright region in Figs. 3 and 4 exhibited an enhancement of $\delta B_z \sim 2$ G [see Fig. 4(b)]. Using the $B_z(x)$ determined above, in the Fig. 4(b) inset we show that the brightening (yellow colored region) in Fig. 3(a) [in Fig. 3(b)] is associated with a change in local vortex density [$= (B_z)/\phi_0$]. With increasing B_a as the vortex density increases, the change in local field becomes smaller as shown in Fig. 4(b). The brightening associated with vortex density increase discussed above, we believe, is related to

vortex melting phase transition wherein a dilute vortex state (VS) melts into a vortex liquid (VL) in a pnictide sample. Subsequently, we argue that the nature of the phase below the liquid at low fields is a disordered low-density glassy vortex solid.

We argue here that further indirect evidence of formation of a vortex liquid phase is via the consideration that there is a redistribution of shielding currents in the sample due to the formation of a VL phase which has a relatively higher dissipation to flow of current (as vortex pinning is nominally zero here) compared to the VS phase, which is a lower dissipation phase (with much higher pinning). Due to this, as the VL phase starts forming at the edges (Fig. 3), the shielding current divides and flows partially along the sample edge and another flows along the VS-VL interface [see schematic in Fig. 2(d)]. Note from Fig. 2(a) that the large B_z near the sample edges shows that the shielding currents do not completely leave the sample edge when a VL puddle is nucleated at the edge. The shielding currents which circulate along the VS-VL interface in the sample interior are responsible for driving vortices away from the interface causing the observed depletion of vortex density at these locations [see the dip feature in Fig. 2(a) and the dark region in Fig. 2(b) in the 30 G image]. Around the edges of the VL puddle, we see the dark contours of the region with depleted vortex density in Fig. 2(b). We believe in these regions the sample has very weak pinning as vortices are driven away from the interface in these regions with shielding currents $\sim 10^{-1}$ A cm⁻² (discussed earlier). As B_a

increases and the region with VL phase expands deeper into the sample, the region with lower B_z (dark contrast around the bright region) moves deeper into the sample. Here we would like to mention that the black line drawn across the sample in Fig. 2(b) is at such a position that the suppressed B_z (dark) region expands along the line for a few different B_a values, with the bright region not crossing the line. Due to this in Fig. 2(a), we observed the suppressed B_z region expand with increasing B_a . Note that other than the interface separating a VL-VS, it is unlikely to observe the above feature of current flowing along the interface causing vortex depletion. For example, consider an interface between two phases where in both phases the vortices are pinned, albeit with different pinning strengths. In this case, as both phases are pinned, there is minimal difference in the resistivity of the two phases, hence currents would not have any reason to channel preferentially only along the interface.

In Fig. 4(c) we determine the melting phase boundary $B_m^{\text{low}}(T)$ correspond to the onset of brightening at the location marked by * in the first figure of Fig. 3(b). We use the criteria of a maxima in $\{\delta B_{z-1}\}$ [see Fig. 4(b)] to identify the location of $B_m^{\text{low}}(T)$ boundary at a given location in the sample. Around the $B_m^{\text{low}}(T)$, in Fig. 4(c) we draw two lines indicating the bounds of the region around the maximum in the $\{\delta B_{z-1}\}(B)$ curve in Fig. 4(b) where $\{\delta B_{z-1}\} > 0$. We shade the region bounded between these two lines around $B_m^{\text{low}}(T)$, as the regime over which a phase transformation occurs. Later on, we compare the $B_m^{\text{low}}(T)$ data with the theoretical predicted low-field melting line equation. In the vortex melting phase diagram of Fig. 4(c) we also show the location of the reversible response of the superconductors [viz., irreversibility line, $B_{\text{irr}}(T)$], determined from the loss of hysteresis in bulk $M(B_a)$ measurements [see Fig. 1(a)]. In a vortex matter phase diagram the location of the boundary across which thermal fluctuations dominate, leading to vortex melting of the solid, is governed by the value of the Ginzburg number (G_i) [1]. For our K-doped 122 sample we estimate $G_i = 1/2 [k_B T_c \gamma / 4\pi B_c^2(0) \xi_{ab}^3(0)]^2 \sim 10^{-3}$ using thermodynamic critical field $B_c(0) [\sim \frac{1}{\kappa} B_{c2}(0)] \sim 1.55$ T (reported [63] upper critical field $B_{c2} \sim 155$ T, $\kappa \sim 100$), ab -axis superconducting coherence length $\xi(0) \sim 1.2$ nm [64], and the estimated anisotropy of our sample is $\gamma \sim 1.22$ (see below). The G_i value for our K-doped single crystal is between that of $\sim 10^{-6} - 10^{-5}$ in low- T_c superconductors and $\sim 10^{-2} - 10^{-1}$ in HTSCs. The relatively large G_i suggests that the vortices in this material are susceptible to thermal fluctuations effects. The olive-colored line in Fig. 4(c) is the line obeying the formula for the high-field melting of a vortex lattice for this pnictide system [1], given as $B_m^{\text{high}}(T) = (5.6c_L^4/G_i)B_{c2}(0)(1 - \frac{T}{T_c(0)})^2$ where $G_i = 10^{-3}$ and a standard Lindemann number c_L of 0.2. We see the $B_m^{\text{high}}(T)$ line coincides with $B_{\text{irr}}(T)$, while the observed VS melting data points $B_m^{\text{low}}(T)$ are well below the $B_m^{\text{high}}(T)$ line. The melting phenomenon at high fields has already been studied in a K-doped 122 pnictide system very similar to ours, viz., in $\text{Ba}_{0.5}\text{K}_{0.5}\text{Fe}_2\text{As}_2$ single crystals, which has a T_c slightly different from ours [32]. In the phase diagram of Fig. 4(c) the data from Ref. [32] are seen to lie on the theoretically predicted $B_m^{\text{high}}(T)$ line [shown as an

olive curve in Fig. 4(c)]. In our phase diagram the $B_m^{\text{high}}(T)$ line is identified as the high-field melting boundary across which thermal fluctuations completely overcome bulk pinning effects in the sample.

We next use scaling analysis used for HTSCs [65–70] to investigate the dimensionality of the vortex state in our pnictide sample. In this analysis isofield $M(T)$ curves measured for our sample at low and high B_a with the appropriate choice of dimensionality D are replotted as $\frac{M}{(TB_a)^{D(D-1)/D}}$ versus $\frac{[T-T_c(B_a)]}{(TB_a)^{D(D-1)/D}}$ [69,70] and all isofield $M(T)$ curves collapse onto a single curve. The scaling analysis we have performed is in a temperature regime close to T_c , viz., $T/T_c(0) < 1\%$, where there is no irreversibility. Figure 5(a) shows $M(T)$ data from low to high fields scaled by choosing $D = 1.2 \pm 0.1$. Figures 5(b) and 5(c) show the absence of scaling with $D = 2$ and 3, respectively. We believe that lowered dimensionality of vortices is due to the presence of naturally present extended pins in our sample. To search further the evidence of extended pins in the sample, we perform angular dependent magnetization measurements. In Fig. 5(d) we see that the width of the hysteresis loop is maximum when $B_a \parallel c$ axis of the single crystal and as we change the angle (θ) between the B_a and crystallographic c axis there is a significant decrease in the width of the loop. The loop width is minimum for $B_a \perp c$ ($\theta = 0^\circ$). By incorporating demagnetization corrections from the width of the irreversible magnetization loop measured for different θ , we determine the J_c^{bulk} vs B_a for two different orientations, viz., $B_a \parallel$ to crystal c axis (maximum demagnetization correction) and $B_a \perp$ to crystal c axis (minimum demagnetization correction). For $\theta = 90^\circ$ ($B_a \parallel$ to crystal c axis) we use $J_c^{\text{bulk}} = 20\Delta M/[a(1 - a/3b)]$ for $b > a$, while for $B_a \perp$ to crystal c axis with the field gradient set up along sample thickness, $J_c^{\text{bulk}} = 20\Delta M/t$, where t is sample thickness. In Fig. 5(e) we see that at low fields, despite including demagnetization corrections the $J_c^{\text{bulk}}(\theta = 90^\circ, B_a \parallel c) \sim 100 J_c^{\text{bulk}}(\theta = 0^\circ, B_a \perp c)$. The significant drop in J_c^{bulk} as the orientation of the sample with respect to B_a is changed from 90° , suggests the presence of extended defects in the sample which are oriented along c axis. In our angular field dependent study of J_c , the pinning and hence J_c becomes maximum for the orientation in which vortices fully align with the extended defects. In our sample, as J_c is maximum for field oriented along the c axis hence the defects extend along the sample c axis (thickness). The $M(B_a)$ in Fig. 5(d) shows that the high J_c^{bulk} (large ΔM) seen in Fig. 1 was due to extended strong pinning in the sample. The hysteresis loop width is much smaller in a direction perpendicular to these defects. We have shown a preferential and directed nature of vortices penetrating into the sample where we believe extended pins are located (see Supplemental Material Fig. 1 [62]). This leads to higher vortex density and consequently a larger local field over these defect planes compared to surrounding regions. The larger local field in these regions of the sample causes the local field to hit the $B_m^{\text{low}}(T)$ value at a given T first, thereby nucleating low-field melting from these regions as seen in Fig. 3. From the $M(B_a)$ loops measured in different orientations we plot the behavior of $B_{c2}(\theta)$ at 35 K (see Supplemental Material Fig. 2 [62]). The fit to $B_{c2}(\theta)$ with the known GL expression

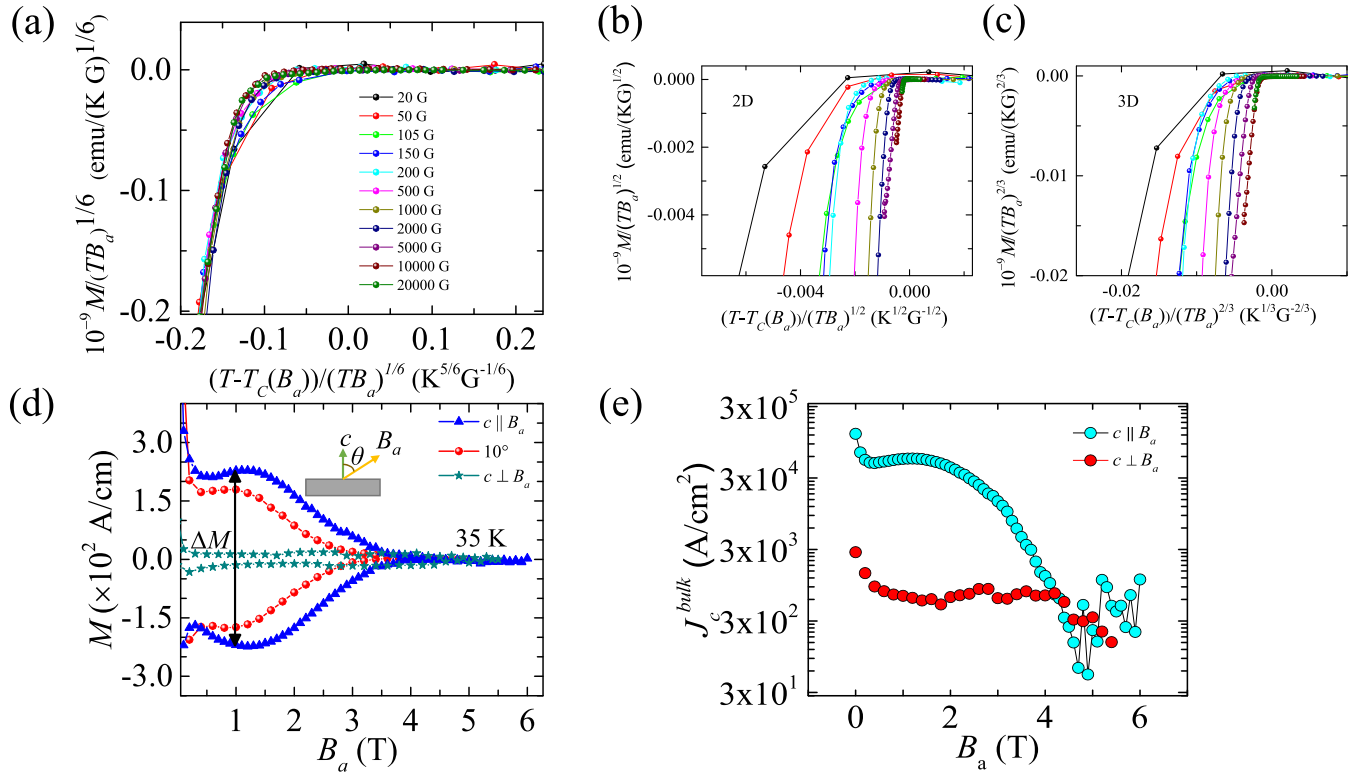


FIG. 5. (a) $M/(TB_a)^{1/6}$ versus $[T - T_c(B_a)]/(TB_a)^{1/6}$ is plotted, obtained from M vs T curves with different applied B as shown in the figure (see text for details). Panels (b) and (c) show that scaling behavior is not followed for two and three dimensions. (d) Angular dependence study of the $M(B_a)$ hysteresis loop, which shows a decrease in the width of the loop with increasing angle with respect to c axis as shown in the schematic. (e) Critical current density J_c^{bulk} vs applied field for orientation $B_a \parallel c$ and $B_a \perp c$ at 35 K. In all the plots from (a) to (e), we have chosen the symbol size comparable to the size of the error bars.

$B_{c2}(\theta) = B_{c2}(\parallel c, T)(\sin^2\theta + \gamma^{-2}\cos^2\theta)^{-1/2}$ [71] gives an estimate of sample anisotropy $\gamma = 1.22 \pm 0.11$. It may be mentioned here that the anisotropy value depends on doping levels in the sample and also on the temperature at which it is determined. Depending on the criteria used to determine H_{c2} from either resistivity or magnetization measurements, there can be some spread in the reported anisotropy values. In similar samples like ours, the anisotropy at lower temperatures is about 2.6 [64].

At low fields (\sim few tens gauss), the intervortex spacing $a_0 \propto (\phi_0/B_a)^{1/2} \gg \lambda$ (~ 200 nm). In this regime, the vortices are weakly interacting as intervortex interactions in this regime go as $\exp(-r/\lambda)$, where r is the spacing between vortices. The weak rigidity of the vortex state at low fields [below the $B_m^{\text{low}}(T)$ boundary in Fig. 4(c)] in the presence of the naturally occurring strong extended pinning centers in the sample results in a dilute glassy phase in our pnictide superconductor below the $B_m^{\text{low}}(T)$ boundary. We identify this phase as the low-field glassy phase in Fig. 4(c), which sustains a finite high critical current. From the location of the low-field melting line in Fig. 4(c), it appears that the low-field glassy vortex phase melts into a vortex liquid phase. We would also like to mention that in our experiments we do not see evidence of melting below $T = 0.4T_c$. Thus, below $0.4T_c$ the glassy vortex phase dominates the low-field portion of the phase diagram. Below $0.4T_c$ the glassy phase obliterates the $B_m^{\text{low}}(T)$ line where at these low T the thermal fluctuations

are insufficient to melt the vortex state. Subsequently we discuss the nature of the vortex phases present above $0.4T_c$. Around the $B_m^{\text{low}}(T)$ line, there is a thermal melting of the glassy vortex state into a dilute vortex liquid. With increasing field or temperature as the melting phenomenon is nucleated in different regions of the sample, the puddles of liquid phase form and spread across the sample [see Fig. 3(b) beyond 12 G]. In Fig. 4(c) we compare the $B_m^{\text{low}}(T)$ melting data points (blue solid circles) with the Lindemann criteria based low-field melting equation shown below [1]:

$$B_m^{\text{low}}(T) \approx \frac{\phi_0}{\lambda^2} \frac{1}{4} \left[\ln \left(\frac{4\pi c_L^2 \epsilon_0 \lambda}{(3\pi)^{1/4} T} \right) \right]^{-2}, \quad (1)$$

where λ is the penetration depth and $\epsilon_0 = (\phi_0/4\pi\lambda)^2$ is the vortex line energy [15]. In Fig. 4(c) the red line is a plot of Eq. (1) using $c_L = 0.14$ [1]. For the plot we have used the penetration depth $\lambda(T)$ determined by fitting the lower critical field $B_{c1}(T)$ behavior we have measured for our sample using $\lambda(T) = \lambda_0/[1 - (T/T_c)^2]^{1/2}$, with $\lambda_0 \approx 200$ nm (see Supplemental Material Fig. 3 [62]). In Fig. 4(c) we see that the theoretically predicted low-field melting line and the experimentally determined $B_m^{\text{low}}(T)$ data closely follow each other with the theoretical curve being slightly lower in field compared to the experimental data. The vortex liquid phase lies below the upper boundary of the liquid phase and a vortex solid exists above it, and the theoretically predicted low-field

melting Eq. (1) seems to be located in the center of the shaded liquid regime in the phase diagram of Fig. 4(c). At very low fields, however, there is a glassy vortex state as shown in our phase diagram. It may be remembered that the theoretically proposed low-field melting line [Eq. (1)], is for an ideal pinning free system. We believe some of these differences from the theoretical low-field melting boundary [1] and the experimental $B_m^{\text{low}}(T)$ data in Fig. 4(c) could be related to the influence of extended defects present in the sample. At very low fields in our sample, we have already suggested the presence of a low-field glassy vortex phase. Around the low-field melting $B_m^{\text{low}}(T)$ line, which obeys the theoretically predicted low-field melting line, one has a liquid phase. At high fields with enhanced interactions between vortices viz., at $a_0 \sim (\phi_0/B)^{1/2} = \lambda(T) = \lambda(0)/[1 - (T/T_c)^2]^{1/2}$, the elastic moduli of the lattice get enhanced and the vortex solid forms across the sample. Using the above criterion of $a_0 = \lambda(T)$ we get the interaction boundary, $B_{\text{int}}(T) = \phi_0[1 - (T/T_c)^2]/\lambda(0)^2$, plotted in Fig. 4(c). Above the $B_{\text{int}}(T)$ boundary, the intervortex interaction dominates the behavior of the vortex matter. We believe that as the interaction dominated regime in the vortex matter phase diagram is approached the observed gradual diminishing of the brightness of the melting patterns in Fig. 3 is related to the VL transforming into a VS phase. In Fig. 4(c) above the shaded region around $B_m^{\text{low}}(T)$, there are no jumps in local B_z , i.e., we observe uniform B_z across the sample (Fig. 2). Due to strong intervortex interactions setting in the vortex state only above $B_{\text{int}}(T)$, the vortex phase above the shaded liquid phase region and below $B_{\text{int}}(T)$ we call a soft vortex solid phase with uniform gradients. Above the $B_{\text{int}}(T)$ line in Fig. 4(c) we identify the rigid vortex solid which finally melts across the high-field melting line, $B_m^{\text{high}}(T)$ and enters a fluctuation dominated regime.

It may be noted that it is only above the $B_{\text{int}}(T)$ theoretical boundary, where intervortex interactions dominate, that we believe the denser quasi-well-ordered rigid vortex solid phase is expected to form. It is worthwhile to note that at high fields of above 200 G in Fig. 3(a), the linear fingerlike projections are no longer visible in the DMO images. We speculate that in the high-field intervortex interaction dominated regime viz., as $B_a \rightarrow B_{\text{int}}$, the effective pinning strength of the linear extended defects weakens. Note that the SMP anomaly in Fig. 1 is observed close to the $B_{\text{int}}(T)$ boundary. Here we estimate the difference in entropy (δS) between a glassy vortex state and vortex liquid phase. For the purpose of this calculation, in the low-field regime where the intervortex interaction is weak, i.e., $B_m < B_{\text{int}}$ and $a_0 > \lambda$, we consider that the shear elastic moduli (c_{66}) of the vortex lattice goes to zero as the lattice melts. Then $\Delta U \approx c_{66}\langle u^2 \rangle$ is the difference in energy of thermally fluctuating vortices as the VS transforms into a VL phase [1, 18] as $c_{66} \rightarrow 0$ in the VL phase and $\langle u^2 \rangle = c_L^2 a_0^2$

for melting. Around the melting line, the difference in entropy as one goes from the VS to VL phase is approximately $\delta S \approx \frac{\Delta U}{T_m} \frac{\delta B_z}{B_z}$, where the temperature of the glassy vortex phase and of the vortex liquid phase near the melting line is approximated with T_m and $\frac{\delta B_z}{B_z} \sim 2 \times 10^{-1}$ is the typical change in the vortex number density near the $B_m^{\text{low}}(T)$. As pnictides possess the Fe_2As_2 layered structure, it is convenient to estimate the entropy difference associated with vortex line segments of length t , where t is the Fe_2As_2 layer spacing ($\sim 6.6 \text{ \AA}$ in our K-doped crystal). Using the above, the estimated δS between the dilute VS and VL phases and using $T_m = 22 \text{ K}$ is

$$\delta S \sim \frac{c_{66}\langle u^2 \rangle t}{T_m} \frac{\delta B_z}{B_z} = \frac{c_{66}c_L^2 a_0^2}{T_m} \frac{\delta B_z}{B_z} = 0.0008k_B,$$

where $c_{66} \approx \frac{\phi_0 B}{[8\pi\lambda(T)]^2}$ [1, 18], $c_L = 0.14$, and $a_0 \sim (\phi_0/B_m)^{1/2}$. The difference in entropy between the low-field glassy vortex solid and vortex liquid phase turns out to be quite small (of the order of $0.001k_B$). Based on this estimate we believe the entropy difference between the low-field glassy vortex solid and liquid phases is far too small to suggest that the low-field melting phase transition around the $B_m^{\text{low}}(T)$ line in Fig. 4(c) is a first-order transition. In the low-field vortex matter phase diagram, around the $B_m^{\text{low}}(T)$ line, we most likely have a second-order phase transformation from a low-field glassy vortex phase into a dilute vortex liquid phase. We find that both the glassy and liquid phases exist well below the intervortex interaction dominated regime which is present above $B_{\text{int}}(T)$ line in the phase diagram. With increasing field the liquid phase transforms into a weakly interacting solid until the $B_{\text{int}}(T)$ line is reached. The strongly interacting vortex solid present above the $B_{\text{int}}(T)$ line finally undergoes a vortex melting transition at high field above $B_m^{\text{high}}(T)$ [32] and enters into a fluctuation dominated phase.

In summary, with this work, we have shown the existence of a low-field vortex liquid phase transition in $\text{Ba}_{0.6}\text{K}_{0.4}\text{Fe}_2\text{As}_2$. The presence of extended pins in the sample leads to formation of a low-field glassy phase which is present prior to its melting into a low-field liquid. It is only at higher fields that the liquid phase solidified into a vortex solid phase. The low-field melting boundary we show obeys the theoretical reentrant, low-field melting line equation. The nature of low-field melting from a glassy phase below it seems to be second-order-like. We hope that our present work will stimulate further theoretical as well as experimental work into better understanding of the rich low-field vortex phase in pnictide superconductors.

ACKNOWLEDGMENT

S.S.B. would like to acknowledge the funding support from IITK (IN) and DST-TSDP (IN), DST-SERB-Imprint II (IN), Government of India.

- [1] G. Blatter, M. V. Fiegl'man, V. B. Geshkenbein, A. I. Larkin, and V. M. Vinokur, *Rev. Mod. Phys.* **66**, 1125 (1994).
 [2] A. A. Abrikosov, *Zh. Eksp. Teor. Fiz.* **32**, 1442 (1957) [*Sov. Phys. JETP* **5**, 1174 (1957)].

- [3] D. R. Nelson, *Phys. Rev. Lett.* **60**, 1973 (1988); D. R. Nelson, and H. S. Seung, *Phys. Rev. B* **39**, 9153 (1989).
 [4] P. L. Gammel, L. F. Schneemeyer, J. V. Waszczak, and D. J. Bishop, *Phys. Rev. Lett.* **61**, 1666 (1988).

- [5] E. H. Brandt, *Phys. Rev. Lett.* **63**, 1106 (1989).
- [6] E. H. Brandt, *Int. J. Mod. Phys. B* **5**, 751 (1991).
- [7] E. H. Brandt, *Rep. Prog. Phys.* **58**, 1465 (1995).
- [8] M. A. Moore, *Phys. Rev. B* **39**, 136 (1989); A. Houghton, R. A. Pelcovits, and A. Sudbø, *ibid.* **40**, 6763 (1989).
- [9] P. L. Gammel, L. F. Schneemeyer, and D. J. Bishop, *Phys. Rev. Lett.* **66**, 953 (1991).
- [10] D. S. Fisher, M. P. A. Fisher, and D. A. Huse, *Phys. Rev. B* **43**, 130 (1991).
- [11] T. Giamarchi and P. Le Doussal, *Phys. Rev. Lett.* **72**, 1530 (1994); *Phys. Rev. B* **52**, 1242 (1995), and references therein.
- [12] M. Gingras and D. A. Huse, *Phys. Rev. B* **53**, 15193 (1996).
- [13] T. Giamarchi and P. Le Doussal, *Spin Glasses and Random Fields*, edited by A. P. Young (World Scientific, Singapore, 1998).
- [14] T. Natterman and S. Scheidl, *Adv. Phys.* **49**, 607 (2000).
- [15] G. Blatter, V. B. Geshkenbein, A. Larkin, and H. Nordborg, *Phys. Rev. B* **54**, 72 (1996).
- [16] G. Blatter and B. Ivlev, *Phys. Rev. B* **50**, 10272 (1994); L. I. Glazman and A. E. Koshelev, *ibid.* **43**, 2835 (1991).
- [17] R. B. van Dover, L. F. Schneemeyer, E. M. Gyorgy, and J. V. Waszczak, *Phys. Rev. B* **39**, 4800(R) (1989); D. E. Farrell, J. P. Rice, and D. M. Ginsberg, *Phys. Rev. Lett.* **67**, 1165 (1991); H. Safar, P. L. Gammel, D. A. Huse, D. J. Bishop, J. P. Rice, and D. M. Ginsberg, *ibid.* **69**, 824 (1992); W. Kwok, J. Fendrich, S. Fleshler, U. Welp, J. Downey, and G. W. Crabtree, *ibid.* **72**, 1092 (1994).
- [18] E. Zeldov, D. Majer, M. Konczykowski, V. B. Geshkenbein, V. M. Vinokur, and H. Shtrikman, *Nature (London)* **375**, 373 (1995).
- [19] A. Schilling, R. A. Fisher, N. E. Phillips, U. Welp, D. Dasgupta, W. K. Kwok, and G. W. Crabtree, *Nature (London)* **382**, 791 (1996).
- [20] S. Colson, M. Konczykowski, M. B. Gaifullin, Y. Matsuda, P. Gierlowski, M. Li, P. H. Kes, and C. J. van der Beek, *Phys. Rev. Lett.* **90**, 137002 (2003).
- [21] S. S. Banerjee *et al.*, *Phys. Rev. Lett.* **90**, 087004 (2003).
- [22] M. J. W. Dodgson, A. E. Koshelev, V. B. Geshkenbein, and G. Blatter, *Phys. Rev. Lett.* **84**, 2698 (2000).
- [23] A. Crisan, S. J. Bending, Z. Z. Li, and H. Raffy, *Supercond. Sci. Technol.* **24**, 115001 (2011).
- [24] G. Shaw, P. Mandal, S. S. Banerjee, and T. Tamegai, *New J. Phys.* **14**, 083042 (2012).
- [25] J. P. Lv and Q. H. Chen, *Phys. Rev. B* **78**, 144507 (2008).
- [26] Q. H. Chen, Q. M. Nie, J. P. Lv, and T. C. Au Yeung, *New J. Phys.* **11**, 035003 (2009).
- [27] N. Avraham *et al.*, *Nature (London)* **411**, 451 (2001).
- [28] Y. Yin, M. Zech, T. L. Williams, X. F. Wang, G. Wu, X. H. Chen, and J. E. Hoffman, *Phys. Rev. Lett.* **102**, 097002 (2009).
- [29] C. L. Song, Y. Yin, M. Zech, T. Williams, M. M. Yee, G. F. Chen, J. L. Luo, N. L. Wang, E. W. Hudson, and J. E. Hoffman, *Phys. Rev. B* **87**, 214519 (2013).
- [30] C. J. van der Beek *et al.*, *Phys. Rev. B* **81**, 174517 (2010).
- [31] L. Shan *et al.*, *Nat. Phys.* **7**, 325 (2011).
- [32] H. K. Mak, P. Burger, L. Cevey, T. Wolf, C. Meingast, and R. Lortz, *Phys. Rev. B* **87**, 214523 (2013).
- [33] T. Taen, F. Ohtake, H. Akiyama, H. Inoue, Y. Sun, S. Pyon, T. Tamegai, and H. Kitamura, *Phys. Rev. B* **88**, 224514 (2013).
- [34] P. Mandal, D. Chowdhury, S. S. Banerjee, and T. Tamegai, *Rev. Sci. Instrum.* **83**, 123906 (2012).
- [35] A. A. Polyanskii, D. M. Feldmann, and D. C. Larbalestier, *Magneto-Optical Characterization Techniques Handbook of Superconducting Materials*, 2nd ed., edited by D. A. Cardwell and D. S. Ginley (Institute of Physics Publishing, Bristol, 2003).
- [36] A. Soibel, E. Zeldov, M. Rappaport, Y. Myasoedov, T. Tamegai, S. Ooi, M. Konczykowski, and V. B. Geshkenbein, *Nature (London)* **406**, 282 (2000); A. Soibel, Y. Myasoedov, M. L. Rappaport, T. Tamegai, S. S. Banerjee, and E. Zeldov, *Phys. Rev. Lett.* **87**, 167001 (2001).
- [37] M. Daeumling, J. M. Seuntjens, and D. C. Larbalestier, *Nature (London)* **346**, 332 (1990); M. F. Goffman, J. A. Herbsommer, F. de la Cruz, T. W. Li, and P. H. Kes, *Phys. Rev. B* **57**, 3663 (1998), and references therein.
- [38] T. Tamegai, Y. Iye, I. Oguro, and K. Kishio, *Physica C* **213**, 33 (1993); B. Khaykovich, E. Zeldov, D. Majer, T. W. Li, P. H. Kes, and M. Konczykowski, *Phys. Rev. Lett.* **76**, 2555 (1996).
- [39] D. Ertas and D. R. Nelson, *Physica C* **272**, 79 (1996).
- [40] B. Khaykovich, M. Konczykowski, E. Zeldov, R. A. Doyle, D. Majer, P. H. Kes, and T. W. Li, *Phys. Rev. B* **56**, 517(R) (1997).
- [41] K. Deligiannis, P. A. J. de Groot, M. Oussena, S. Pinfold, R. Langan, R. Gangon, and L. Taillefer, *Phys. Rev. Lett.* **79**, 2121 (1997); H. Küpfer, Th. Wolf, C. Lessing, A. A. Zhukov, X. Lancon, R. Meier-Hirmer, W. Schauer, and H. Wühl, *Phys. Rev. B* **58**, 2886 (1998); S. Okayasu, and H. Asaoka, *Physica C* **317-318**, 633 (1999).
- [42] D. Giller, A. Shaulov, R. Prozorov, Y. Abulafia, Y. Wolfus, L. Burlachkov, Y. Yeshurun, E. Zeldov, V. M. Vinokur, J. L. Peng, and R. L. Greene, *Phys. Rev. Lett.* **79**, 2542 (1997).
- [43] T. Nishizaki, T. Naito, and N. Kobayashi, *Phys. Rev. B* **58**, 11169 (1998); *Physica C* **317-318**, 645 (1999).
- [44] D. Giller, A. Shaulov, Y. Yeshurun, and J. Giapintzakis, *Phys. Rev. B* **60**, 106 (1999).
- [45] S. Kokkaliaris, P. A. J. de Groot, S. N. Gordeev, A. A. Zhukov, R. Gagnon, and L. Taillefer, *Phys. Rev. Lett.* **82**, 5116 (1999).
- [46] S. S. Banerjee *et al.*, *Phys. Rev. B* **62**, 11838 (2000).
- [47] S. Mohan, J. Sinha, S. S. Banerjee, and Y. Myasoedov, *Phys. Rev. Lett.* **98**, 027003 (2007).
- [48] H. Yang, H. Q. Luo, Z. S. Wang, and H. H. Wen, *Appl. Phys. Lett.* **93**, 142506 (2008).
- [49] S. Demirdiř, C. J. van der Beek, S. Mühlbauer, Y. Su, and T. Wolf, *J. Phys.: Condens. Matter* **28**, 425701 (2016).
- [50] R. Prozorov, N. Ni, M. A. Tanatar, V. G. Kogan, R. T. Gordon, C. Martin, E. C. Blomberg, P. Proumapan, J. Q. Yan, S. L. Bud'ko, and P. C. Canfield, *Phys. Rev. B* **78**, 224506 (2008).
- [51] R. Prozorov, M. A. Tanatar, E. C. Blomberg, P. Proumapan, R. T. Gordon, N. Ni, S. L. Bud'ko, and P. C. Canfield, *Physica C* **469**, 667 (2009).
- [52] R. Prozorov, M. A. Tanatar, N. Ni, A. Kreyssig, S. Nandi, S. L. Bud'ko, A. I. Goldman, and P. C. Canfield, *Phys. Rev. B* **80**, 174517 (2009).
- [53] Y. Nakajima, Y. Tsuchiya, T. Taen, T. Tamegai, S. Okayasu, and M. Sasase, *Phys. Rev. B* **80**, 012510 (2009).
- [54] C. P. Bean, *Rev. Mod. Phys.* **36**, 31 (1964).
- [55] H. P. Wiesinger, F. M. Sauerzopf, and H. W. Weber, *Physica C* **203**, 121 (2003).
- [56] E. Zeldov, A. I. Larkin, V. B. Geshkenbein, M. Konczykowski, D. Majer, B. Khaykovich, V. M. Vinokur, and H. Shtrikman, *Phys. Rev. Lett.* **73**, 1428 (1994).

- [57] B. Khaykovich, M. Konczykowski, K. Teitelbaum, E. Zeldov, H. Shtrikman, and M. Rappaport, *Phys. Rev. B* **57**, 14088(R) (1998).
- [58] E. H. Brandt, *Phys. Rev. B* **59**, 3369 (1999).
- [59] R. J. Wijngaarden, K. Heeck, H. J. W. Spoelder, R. Surdeanu, and R. Griessen, *Physica C* **295**, 177 (1998).
- [60] E. H. Brandt, G. P. Mikitik, and E. Zeldov, *J. Exp. Theor. Phys.* **117**, 439 (2013).
- [61] P. E. Goa, H. Hauglin, A. A. F. Olsen, D. Shantsev, and T. H. Johansen, *Appl. Phys. Lett.* **82**, 79 (2003).
- [62] See Supplemental Material at <http://link.aps.org/supplemental/10.1103/PhysRevB.101.014502> for additional data on the vortex phase diagram and a movie of the low-field vortex lattice melting phenomenon.
- [63] U. Welp, R. Xie, A. E. Koshelev, W. K. Kwok, H. Q. Luo, Z. S. Wang, G. Mu, and H. H. Wen, *Phys. Rev. B* **79**, 094505 (2009).
- [64] A. Gurevich, *Rep. Prog. Phys.* **74**, 124501 (2011).
- [65] U. Welp, S. Fleshier, W. K. Kwok, R. A. Klemm, V. M. Vinokur, J. Downey, B. Veal, and G. W. Crabtree, *Phys. Rev. Lett.* **67**, 3180 (1991).
- [66] Z. Tesanovic, L. Xing, L. Bulaevskii, Q. Li, and M. Suenaga, *Phys. Rev. Lett.* **69**, 3563 (1992).
- [67] Q. Li, K. Shibusaki, M. Suenaga, I. Shigaki, and R. Ogawa, *Phys. Rev. B* **48**, 9877 (1993).
- [68] A. Wahl, V. Hardy, F. Warmont, A. Maignan, M. P. Delamare, and Ch. Simon, *Phys. Rev. B* **55**, 3929 (1997).
- [69] B. Rosenstein, B. Ya. Shapiro, R. Prozorov, A. Shaulov, and Y. Yeshurun, *Phys. Rev. B* **63**, 134501 (2001).
- [70] S. Salem-Sugui, L. Ghivelder, A. D. Alvarenga, J. L. Pimentel, H. Luo, Zh. Wang, and H. H. Wen, *Phys. Rev. B* **80**, 014518 (2009).
- [71] M. Tinkham, *Introduction to Superconductivity*, 2nd ed. (Mc Graw-Hill, New York, 1996).